MATERIALS CHEMISTRY FRONTIERS

CCS 中国化学会 CHINESE CHEMICAL SOCIETY

ICCAS

ROYAL SOCIETY OF CHEMISTRY

Hydrophobic pockets built in polymer micelles to enhance reactivity of Cu2+ ions

Journal:	*Materials Chemistry Frontiers*
Manuscript ID	QM-RES-01-2023-000110
Article Type:	Research Article
Date Submitted by the Author:	31-Jan-2023
Complete List of Authors:	Wei, Zichao; University of Connecticut, Department of Chemistry Liu, Chung-Hao; University of Connecticut, Polymer Program, Institute of Materials Science Luo, Qiang; University of Connecticut, Department of Chemistry Thanneeru, Srinivas; University of Connecticut, Chemistry Angeles-Boza, Alfredo; University of Connecticut, Chemistry Nieh, Mu-Ping; University of Connecticut, Chemical and Biomolecular Engineering; University of Connecticut, Polymer Program, Institute of Materials Science He, Jie; University of Connecticut, Department of Chemistry

COMMUNICATION

Hydrophobic pockets built in polymer micelles to enhance reactivity of Cu^{2+} ions

Received 00th January 20xx,
Accepted 00th January 20xx

DOI: 10.1039/x0xx00000x

Zichao Wei,[a] Chung-Hao Liu,[b] Qiang Luo,[a] Srinivas Thanneeru,[a] Alfredo M. Angeles-Boza,[a] Mu-Ping Nieh,[b,c] and Jie He[a,b,*]

Abstract: We report hydrophobicity-enhanced reactivity of Cu^{2+} ions as an ester hydrolase. Using a dipicolyamine (DPA) containing reversible addition-fragmentation chain transfer agent, the synthetic sequence, either hydrophobic or hydrophilic first in amphiphilic block copolymers of polystyrene-*block*-poly(*N'N*-dimethylacrylamide) (PS-*b*-PDMA), is used to vary the physical location of the binding motif, DPA, as confirmed by small-angle X-ray scattering and NMR titrations. The hydrophobicity of Cu^{2+} sites show a significant impact (as large as 60 times more activity) on their catalytic efficiency towards ester hydrolase. With two different kinetic modes including Michaelis-Menten and the reverse saturation kinetics models, the binding constant K_b of substrates to Cu^{2+} sites are quantitatively analyzed and we demonstrate that hydrophobicity favors the binding of substrates to Cu^{2+} sites at polymer micelles with smaller sizes; however, K_b decays exponentially with micellar diameters. Despite of the diffusion barrier, hydrophobicity shows a profound impact on the catalytic rate constant k_c that measures the single conversion rate of bound substrates to products. There is a 16-20 times kinetic enhancement in the hydrolase activity, completely endowed by the hydrophobic microenvironment of Cu^{2+} sites as compared to micelles with similar sizes. Our results on how the hydrophobicity of Cu^{2+}-containing micelles can impact the catalytic efficiency and potentially illustrate a promising way toward the design of bioinspired catalysts.

1. Introduction

Design of synthetic catalysts by taking inspiration from natural and biological processes is promising for next-generation catalysts with high efficiency. In biological enzymes, their co-factors or so-called active sites are usually hidden within well-folded, secondary/tertiary structures of the protein framework.[1] Non-covalent interaction, like metal-ligand binding,[2-4] hydrogen bonding,[5-6] and hydrophobic association,[7-10] can be used to provide channels and proximity to substrates with highly efficient binding/debinding. The utilization of natural enzymes for many organic reactions, however, is very limited due to low stability, poor recyclability and solubility under non-aqueous and high-temperature conditions.[11] As inspired by nature, extensive efforts have been contributed to create synthetic metallopolymer catalysts with a microenvironment for catalytic sites (often metal ions or nanoparticles), such as micelles,[12-17] single chain polymer nanoparticles (SCNPs)[18-29] and dendrimers.[30-33] Among those, polymer micelles have unique nanostructures derived from amphiphilic block polymers (BCPs) of which the hydrophobic segment spontaneously aggregates to form core-shell assemblies in water. Micelles, to some extent, can mimic the biological environment in enzymes because they provide a medium to bridge between water solubility and apolar interior made of hydrophobicity polymers. A hydrophobic pocket that envelops a hydrated substrate has been hypothesized to be a key characteristic of primeval enzymes.[34-37] Therefore, polymer micelles can improve the compatibility and solubility of apolar substrates to enhance reactivity and improve selectivity of some reactions, such as Heck coupling in water.[38]

The core-shell structure of micelles is similar to the biological membranes that mediate the reaction equilibria and reactivity by confining active sites in hydrophobic microenvironment. For example, functionalized lipophiles can bind with transition metal ions,[39-41] like zinc (Zn^{2+}) and copper (Cu^{2+}) ions, to form the metallomicelles and catalyze highly efficient ester hydrolysis.[42] At the same time, control of the chiral structure of lipophilic molecules can lead to the production of enantioselectivity and the differentiation of substrate with the bilayer amphiphilic aggregates. Other organic reactions limited by the low solubility in water can be conducted in the presence of metallomicelles, *e.g.,* hydrogenation reaction[43-44], Diels-Alder reaction[45], and aldol reactions.[46] However, lipids are dynamic and small amphiphiles that usually cannot overwrite the strong hydration of metal ions, *i.e.,* to force metal ions out from aqueous solution. On the other hand, polymer micelles are much larger and less dynamic as compared to those of lipids. Catalytic

[a] *Department of Chemistry, University of Connecticut, Storrs, CT 06269, United State.* Email: jie.he@uconn.edu
[b] *Polymer Program, Institute of Materials Science, University of Connecticut, Storrs, CT 06269, United State*
[c] *Department of Chemical and Biomolecular Engineering, University of Connecticut, Storrs, CT 06269, United State*

Electronic Supplementary Information (ESI) available: Synthetic and characterization details of polymers, kinetic analysis of all polymer micelles, SAXS modeling of polymers, are TEM images. See DOI: 10.1039/x0xx00000x

metal sites can be incorporated into polymer micelles through metal-ligand coordination at a specific solvation environment. Despite being catalytically inactive, previous literatures have suggested that polymer frameworks could show a positive impact on chemical reactions.[47-52] The reactivity enhancement has been attributed to three functionalities from the hydrophobic domain in catalysis; i) the presence of the hydrophobic pocket that can provide the shield for the unstable metals, *e.g.*, Pd NPs catalyzed Suzuki coupling reaction[53-56]; ii) the hydrophobic domain that increases the affinity between non-polar substrates and catalyst via hydrophobic association[57-58]; iii) incorporating the hydrophobic domain near the active sites can screen the size and polarity of substrate thus improving the reaction selectivity.[59-60] Since the design of the micellar catalysts is mainly focused on the high reaction efficiency with multiple anchoring groups and recyclability. The mechanistic studies on how the hydrophobic domain affects the catalytic efficiency of the active sites in synthetic polymer micelles has not been explored.

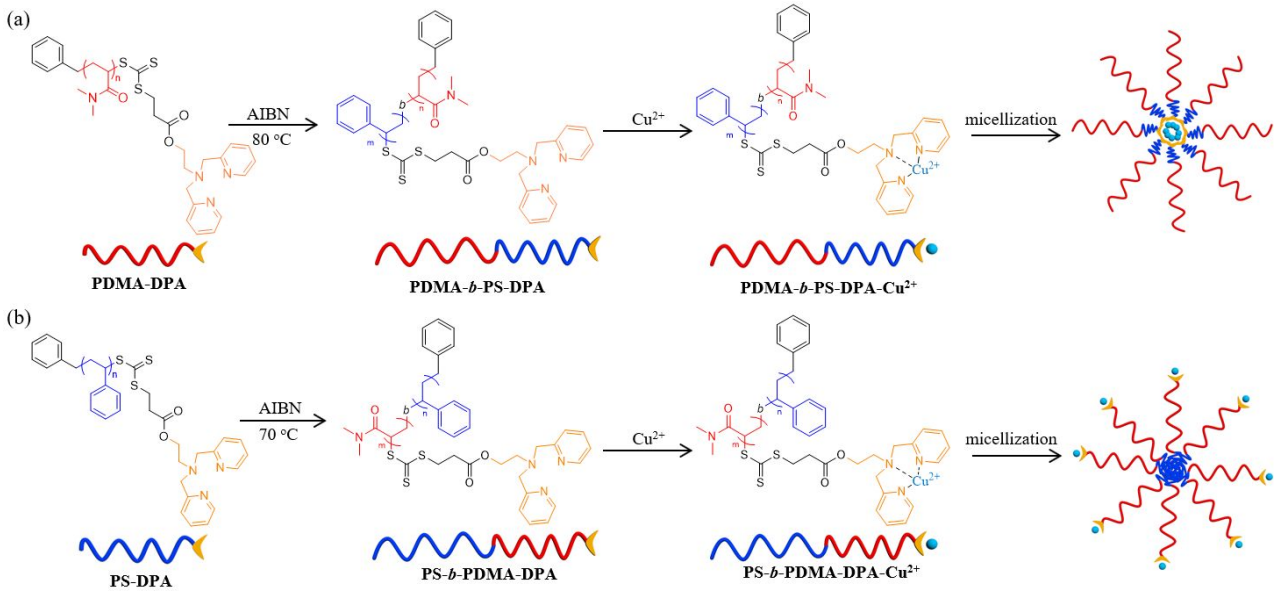

Scheme 1. Chemical structures and synthesis of amphiphilic BCPs of PDMA-*b*-PS and Cu^{2+}-containing micelles with their micellar structures to highlight the location of Cu^{2+} ions: (a) PDMA-*b*-PS-DPA and (b) PS-*b*-PDMA-DPA.

We herein report Cu^{2+}-containing polymer micelles with different locations of active sites that impact the activity of Cu^{2+} ions on hydrolysis reaction. Our synthetic strategy is to control the coordination motif (dipicolyamine, DPA) of Cu^{2+} ions by varying the synthetic sequence, either at the end of hydrophobic or hydrophilic blocks, thereby defining the hydrophobicity of Cu^{2+} sites. We designed a DPA-containing reversible addition-fragmentation chain transfer (RAFT) agent to prepare a series of amphiphilic BCPs of polystyrene-*block*-poly(*N'N*-dimethylacrylamide) (PS-*b*-PDMA) (Scheme 1). These BCPs could self-assemble into uniform micelles in methanol. The size and uniformity of micelles as well as the location of Cu^{2+} ions were confirmed by small-angle X-ray scattering (SAXS) outcomes. Using the titration experiment with D_2O in ^1H NMR, we demonstrated that the binding motif DPA could precisely determine the physical location of metal ions within or outside of micellar cores. The hydrolase activities of Cu^{2+}-containing micelles were examined using the cleavage of *p*-nitrophenyl picolinate (PNPP) as a model reaction. Cu^{2+}-containing micelles. As compared to Cu^{2+}-containing linear hydrophilic PDMA or polymer micelles with Cu^{2+} ions on the hydrophilic shell, an activity enhancement of 58-fold was seen when Cu^{2+} ions were confined in hydrophobic domains with a small radius. We investigated the cooperativity and strong binding affinity for substrates through saturation kinetics and Michaelis–Menten kinetics. The small hydrophobic domains of polymer micelles were found to provide a microenvironment to enhance binding of substrate; while, polymer micelles with large core sizes created a large thermodynamic barrier to limit the initial binding, about two orders of magnitude slower. Our study highlights the importance of micellar microenvironment to tune the activity of metal sites, potentially providing new insights into design of bioinspired catalysts.

2. Results and Discussion

All polymers were prepared through RAFT polymerization. We designed a dipicolyamine-containing RAFT chain transfer agent (CTA) through the coupling reaction of 2-(bis(pyrid-2-ylmethyl)-*N*-(2-hydroxyethyl)-amine (DPA-OH) and 3-benzylsulfinyl thiocarbonyl sulfanyl-propionic acid (BCTPA) as shown in Figure S1. To accurately control the hydrophobicity for the active center, we prepared two types of amphiphilic BCPs to add the binding motif at the end of hydrophobic or hydrophilic segments, respectively. Typically, the polymerizations of styrene (St) and *N'N*-dimethylacrylamide (DMA) were carried out in the presence of azobisisobutyronitrile (AIBN) as an initiator and DPA-BCTPA as the RAFT agent in anisole (Figure S2). The molecular weights of PS and PDMA were controlled by varying the molar ratio between monomer and BTCPA-DPA. The molecular weight (M_n) and polymer dispersity (Đ) of PS/PDMA measured using gel permission chromatography (GPC) and NMR calibrated with PS are summarized in Table 1. In ^1H NMR, the number of repeat units of PS/PDMA was calculated using pyridinyl peaks of DPA at 8.5 ppm as an integration internal standard (Figures S3-S4).

COMMUNICATION

Table 1. Synthesis and characterization details of homopolymers and BCPs.

Sample	Composition	M_w (kg/mol)		Dispersity (M_w/M_n)	D from TEM (nm)	D from SAXS (nm)	Aggregation number (N_{agg})*	Cu^{2+} per core volume (nm^{-3})*
		$M_{n,NMR}$	$M_{n,GPC}$					
PDMA-RAFT	$PDMA_{52}$-DPA	5.6	6.2	1.2	-	-	-	
P1	$PDMA_{52}$-*b*-PS_{10}-DPA	6.7	7.0	1.3	-	8.4±0.4	185	0.6
P2	$PDMA_{52}$-*b*-PS_{20}-DPA	7.7	8.2	1.3	-	9.6±0.2	139	0.3
P3	$PDMA_{52}$-*b*-PS_{52}-DPA	11.2	12.1	1.3	13.4±1.5	12.5±0.2	118	0.1
P4	$PDMA_{52}$-*b*-PS_{76}-DPA	13.6	13.1	1.3	15.2±1.2	14.6±0.2	128	0.08
P5	$PDMA_{52}$-*b*-PS_{105}-DPA	16.1	15.6	1.3	23.1±2.4	21.0±0.2	276	0.05
PS-RAFT	PS_{76}-DPA	8.4	6.9	1.3	-	-	-	
P6	PS_{76}-*b*-$PDMA_{59}$-DPA	14.3	14.3	1.2	14.5±1.5	14.0±0.2	113	-
P7	PS_{76}-*b*-$PDMA_{85}$-DPA	16.8	16.5	1.2	14.3±1.4	13.1±0.2	93	-

*Note: $N_{agg} = (4\pi/3)\times R_{core}^3/(V_s N_{ps})$, where V_s is the volume per polystyrene repeat unit (0.167 nm^3), N_{PS} is the repeat unit of PS block and R_{core} is the radius of micelle cores measured from SAXS. The density of Cu^{2+} ions is calculated as $1/(V_s N_{ps})$.

Using the macro-CTA of PS-DPA/PDMA-DPA, the di-BCPs were synthesized as shown in Scheme 1. For example, the BCPs of PDMA-*b*-PS were synthesized using PDMA-DPA as a macro-CTA. The binding motif can be controlled precisely at the end of the PS segments as PDMA-*b*-PS-DPA. The M_n and Đ of BCPs are summarized in Table 1. From ^1H NMR, the number of repeat units of PS was determined using the protons at 2.8–3.3 ppm of the PDMA as the integration standards. To avoid the impact of nanostructures, all samples have a fairly long PDMA block and a short hydrophobic PS block, likely led to the formation of spherical micelles. The binding motif at the end of the PDMA was synthesized similarly with a PS macro-CTA agent as P6 and P7 in Table 1.

The metal-ligand interaction between Cu^{2+} ions with DPA was first confirmed using UV-vis spectroscopy. Taking PS_{76}-DPA as an example, we titrated its solution in dimethylformamide (DMF) (5 mg mL^{-1}) with $Cu(NO_3)_2$. Figure 1a shows the typical UV-vis absorption spectra at different concentrations of $Cu(NO_3)_2$. The characteristic peak at ~ 650 nm corresponds to the *d-d* transition of Cu^{2+} ions bound with the N-containing ligand, *i.e.,* DPA.[47, 61-62] The peak intensity continuously increased with increasing the concentration of $Cu(NO_3)_2$ and then saturated with a red shift to 650 nm. The absorbance at 650 nm was plotted against the molar ratio of Cu^{2+}-To-DPA as given in Figure 1b. The absorbance reached a plateau at a Cu^{2+}-to-DPA ratio of 1:1. This suggests that the coordination number of Cu^{2+} ions to DPA is approximately one as that presented in molecular complexes.

We further studied the micellization of BCPs in the presence of Cu^{2+} ions using light scattering. Cu^{2+}-coordinated BCPs were first dissolved in DMF with a concentration of 1.5 mg mL^{-1}. The solution was then dialyzed against water to remove DMF and the final micelle concentration was ~1 mg mL^{-1}. The solution was diluted to different concentrations in the range of 0.001 to 1 mg mL^{-1} and the corresponding scattering intensity was measured using dynamic light scattering (DLS, Figure 1c). The critical micelle concentration (CMC) of BCPs was defined as the abrupt turning point of the scattering intensity. The CMCs of $PDMA_{52}$-*b*-PS_{52}-DPA-Cu^{2+} (P3-Cu^{2+}) and PS_{76}-*b*-$PDMA_{59}$-DPA-Cu^{2+} (P6-Cu^{2+}) are 0.038 mg mL^{-1} and 0.039 mg mL^{-1}, respectively. Those values are close to that of PS reported in previous literatures.[63] The presence of Cu^{2+} ions did not vary self-assembly behavior of polymers, regardless of its physical location in micelles.

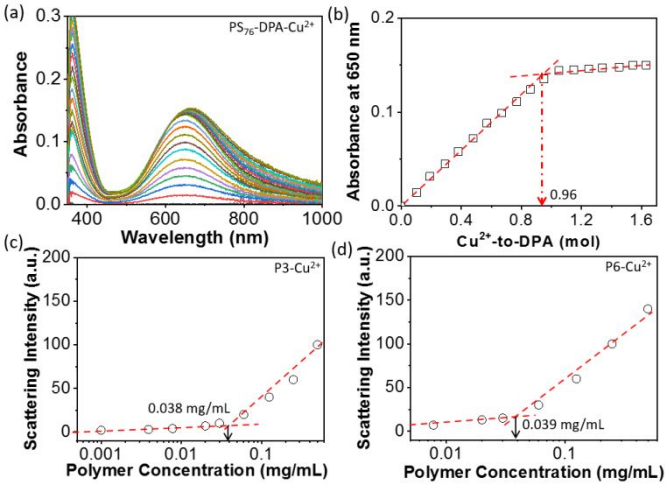

Figure 1. (a) UV-vis spectra to show the titration of PS-DPA with $Cu(NO_3)_2$ measured in DMF. (b) The plot to show adsorption intensity at 650 nm *vs* Cu^{2+}-To-DPA. The concentration of PS-DPA in DMF is 0.59 mM polymer. (c) CMC of P3 and P6 measured by DLS by varying polymer concentration from 0.001 mg mL^{-1} to 1 mg mL^{-1}.

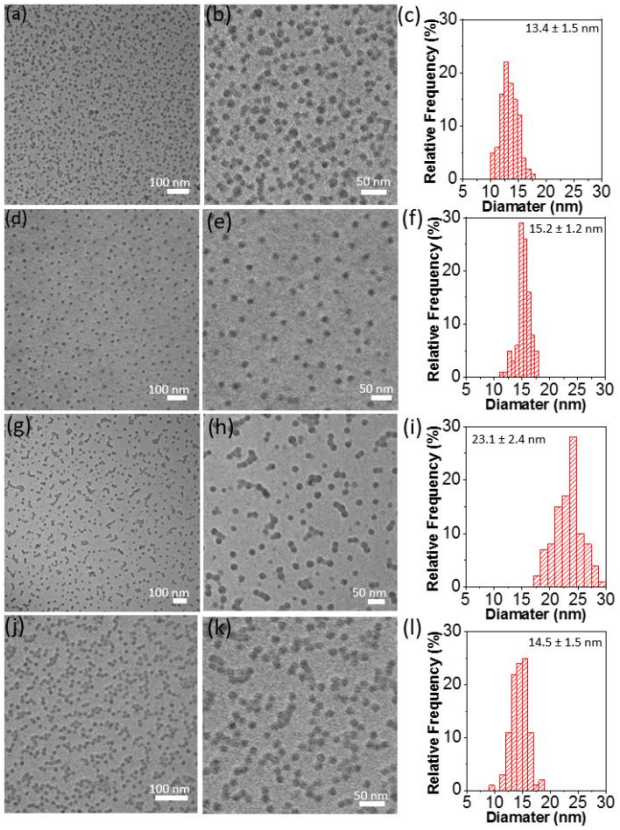

Figure 2. Representative TEM images Cu^{2+}-containing micelles of (a,b) P3, (d,e) P4, (g,h) P5 and (j,k) P6. And the histogram of the average diameter of Cu^{2+}-containing micelles of (c) P3, (f) P4, (i) P5 and (l) P6, respectively.

To prepare monodispersed polymer micelles that avoid the impact of nanostructures on the catalytic activity of Cu^{2+} ions, we examined the thermal annealing method. In methanol, all BCPs of PDMA-*b*-PS were found to form spherical micelles with a narrow size distribution. PDMA-*b*-PS was refluxed in methanol at a concentration of 10 mg mL^{-1}. The solution became clear after a few minutes and $Cu(NO_3)_2$ was added to the solution with the same equivalence of DPA. After thermal annealing for 30 minutes, the solution was cooled back to room temperature. Figures 2 and S5 show the typical transmission electron microscopy (TEM) images of P3-P7. When the repeat unit of PS increased, the micellar diameter increased significantly. The micellar size of P3 of $PDMA_{52}$-*b*-PS_{52}-DPA increases to 13.4 nm; while P6 of PS_{76}-*b*-$PDMA_{59}$-DPA has a core diameter of 14.5 nm. Importantly, the size of micelles is very uniform throughout as confirmed by the histogram analysis of TEM. Note, the micelles of P1 and P2 are too small to be accurately characterized under TEM. Thus, we used SAXS to measure the micellar size of P1-Cu^{2+} and P2-Cu^{2+}. For P1 and P2 with Cu^{2+} ions. The scattering profile fits well as a spherical model (form factor) with a structure factor described by the Hayter-Penfold mean spherical approximation (H-PMSA),[64-65] which explains the broad peak at q ~0.03 $Å^{-1}$ (Figure 3a). As a result of short hydrophobic blocks, the PDMA was presumably strongly hydrated in the shell, leading to insignificant contrast in electron density between the shell and solvent. However, the high-q (e.g., q > 0.1 $Å^{-1}$) scattering intensity can be scaled as $I \sim$ between q^{-2} and $q^{-1.6}$ implying that the PDMA of P1 and P2 (either in shell or in the form of unimer) can be described as a polymer chain. Therefore, the SAXS data of P1-Cu^{2+} and P2-Cu^{2+} are best fitted by a combined model of sphere and Gaussian chain (Figure 3a), yielding the best-fit diameters of 8.4 nm and 9.6 nm respectively, which may exclude the nearly fully hydrated shell thickness due to the low contrast between the shell and solvent (Figure 3b and Table S1).

SAXS measurements were also for Cu^{2+}-containing micelles of P3-P7 (see the summary in Tables S1 and S2). Those samples have the scattering feature (oscillations) of well-defined core-shell spheres (CSS) at the low q regime (q < 0.1 $Å^{-1}$) sitting on the scattering background of $q^{-1.6}$ dependence as q > 0.1 $Å^{-1}$ (presumably swollen polymer chains). Therefore, the SAXS data are best-fitted with a combined CSS and excluded polymer chain model, and the best-fitting dimensions are summarized in Tables S1 and S2. The size of their micellar cores from SAXS is in a close agreement with TEM results. For example, P3 and P6 have a core diameter of 12.5 nm and 14 nm, respectively, as best fitted with the CSS model (Figures 3c and 3d) and the diameter of their micelles from TEM is 13.4 nm and 14.5 nm, respectively.

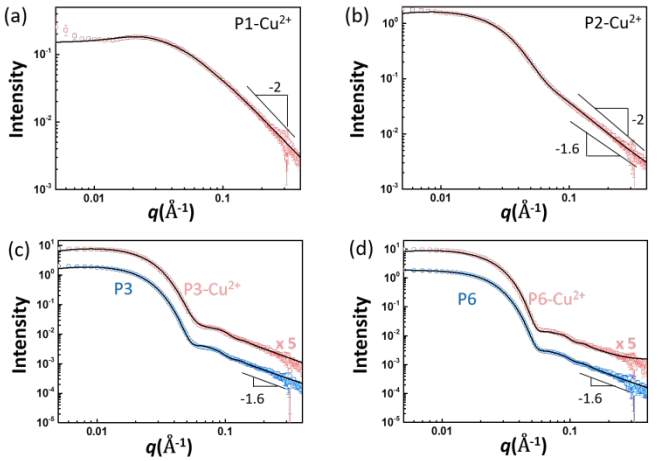

Figure 3. SAXS patterns of polymer micelles of (a) P1-Cu^{2+}; (b) P2-Cu^{2+}; (c) P3 and P3-Cu^{2+}; and (d) P6 and P6-Cu^{2+}.

Since Cu^{2+} ions have a higher electron scattering length density (SLD), we could further use the absolute scattering intensity to identify the physical location of Cu^{2+} ions. We compared the of polymer micelles with *vs.* without Cu^{2+} ions. While Cu^{2+} ions had a minimum impact on the size of polymer micelles, the SLD of the core (ρ_{core}) for Cu^{2+}-containing P3 micelles increased from 9.48×10^{-6} $Å^{-2}$ to 9.62×10^{-6} $Å^{-2}$; whereas, that of the shell (ρ_{shell}) remained the same (Table S2). The slightly higher ρ_{core} can be attributed to the presence of Cu^{2+} ions. In comparison, the ρ_{core} of Cu^{2+}-containing P6 micelles is identical to that of P6 micelles in the absence of Cu^{2+} ions; that is, the ρ_{core} is independent from Cu^{2+} ions. In both cases, no scattering correlation was observed at the high q range, suggesting the uniform distribution of Cu^{2+} ions in the micellar cores (P3) or on the surface of micellar shells (P6).

We further examined the physical location of Cu^{2+} ions using ^1H NMR. After dissolved in d_6-acetone with a concentration of 0.65 mM, Figure 4 displays the NMR spectra of P3 and P6. The peaks at 8.5, 7.7, and 7.6 ppm were assigned to pyridinyl protons of DPA (peaks *a, c* and *d*, respectively), along with the broad peaks of styrene phenyl rings at 6.5-7.5 ppm. When adding $Zn(NO_3)_2$ at the same equivalence to DPA, there was an obvious shift of pyridinyl protons. It should be noted that Cu^{2+} is paramagnetic and diamagnetic Zn^{2+} is used for NMR experiments. The peak *a* at 8.5 ppm shifted to 8.8 ppm, and peaks *c* and *d* shifted to 8.3 and 7.8 ppm, respectively. In presence of 20 vol% D_2O, the phenyl proton peaks of PS in $PDMA_{52}$-*b*-PS_{52}-DPA-Zn^{2+} (P3) and PS_{76}-*b*-$PDMA_{52}$-DPA-Zn^{2+} (P6) became evidently

broadened and less pronounced, suggesting the collapse of hydrophobic PS chains to drive the formation of micelles. When the concentration of D_2O increased to 40 vol%, all phenyl proton peaks of PS disappeared for P3 and P6. In all cases, the protons of hydrophilic PDMA at around 3.0 ppm were well-preserved. In the meanwhile, the pyridyl peaks of DPA in P3 (Figure 4b) disappeared along with PS protons. Interestingly, the peak *g* at 7.0 ppm of the RAFT agent linked to the PDMA end retained. In contrast, the pyridyl peaks of DPA remained in P6 with 40 vol% of D_2O; even no phenyl peaks associated with PS were seen. Those results suggest that the binding motif DPA could collapse with the hydrophobic PS blocks during micellization, if DPA is at the hydrophobic end; whereas, it would remine hydrated if DPA is tied at the hydrophilic end. Together with SAXS results, the microenvironment of Cu^{2+} ions could be defined within those Cu^{2+}-containing micelles of amphiphilic BCPs.

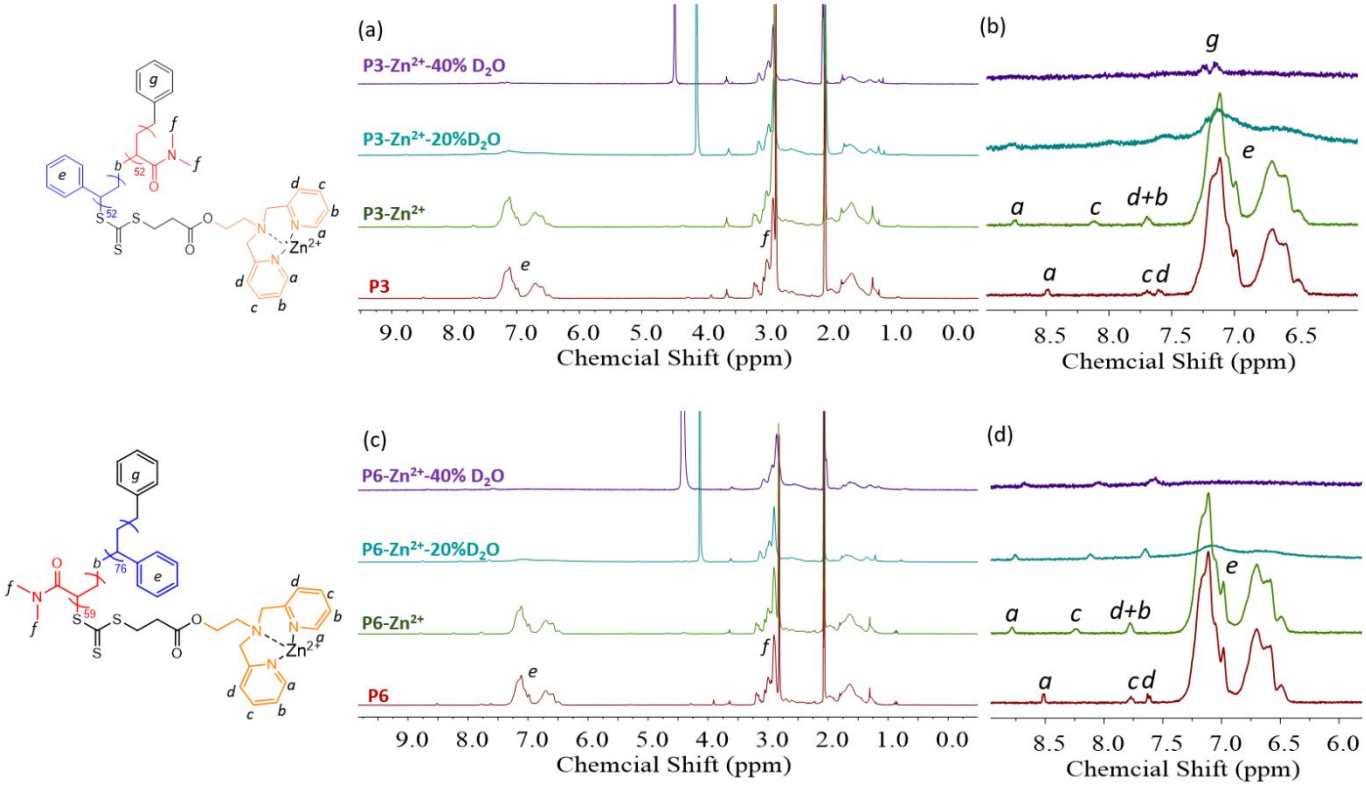

Figure 4. ^1H NMR spectra of (a) P3 and (c) P6 in mixed solvents of D_2O/d_6-acetone. From bottom to top, P3/P6 (red), P3/P6-Zn^{2+}-0% D_2O (green), 20 % D_2O (blue), and 40% D_2O (purple) of D_2O in d_6-acetone. All spectra were recorded with $Zn(NO_3)_2$ to avoid paramagnetic Cu^{2+} ions. Aromatic protons in the range of 6.0 to 9.0 ppm for (b) P3 and (d) P6 demonstrate the difference in the solvation state of DPA.

We further examined the physical location of Cu^{2+} ions using ^1H NMR. After dissolved in d_6-acetone with a concentration of 0.65 mM, Figure 4 displays the NMR spectra of P3 and P6. The peaks at 8.5, 7.7, and 7.6 ppm were assigned to pyridinyl protons of DPA (peaks *a, c* and *d*, respectively), along with the broad peaks of styrene phenyl rings at 6.5-7.5 ppm. When adding $Zn(NO_3)_2$ at the same equivalence to DPA, there was an obvious shift of pyridinyl protons. It should be noted that Cu^{2+} is paramagnetic and diamagnetic Zn^{2+} is used for NMR experiments. The peak *a* at 8.5 ppm shifted to 8.8 ppm, and peaks *c* and *d* shifted to 8.3 and 7.8 ppm, respectively. In presence of 20 vol% D_2O, the phenyl proton peaks of PS in $PDMA_{52}$-*b*-PS_{52}-DPA-Zn^{2+} (P3) and PS_{76}-*b*-$PDMA_{52}$-DPA-Zn^{2+} (P6) became evidently broadened and less pronounced, suggesting the collapse of hydrophobic PS chains to drive the formation of micelles. When the concentration of D_2O increased to 40 vol%, all phenyl proton peaks of PS disappeared for P3 and P6. In all cases, the protons of hydrophilic PDMA at around 3.0 ppm were well-preserved. In the meanwhile, the pyridyl peaks of DPA in P3 (Figure 4b) disappeared along with PS protons. Interestingly, the peak *g* at 7.0 ppm of the RAFT agent linked to the PDMA end retained. In contrast, the pyridyl peaks of DPA remained in P6 with 40 vol% of D_2O; even no phenyl peaks associated with PS were seen. Those results suggest that the binding motif DPA could collapse with the hydrophobic PS blocks during micellization, if DPA is at the hydrophobic end; whereas, it would remine hydrated if DPA is tied at the hydrophilic end. Together with SAXS results, the microenvironment of Cu^{2+} ions could be defined within those Cu^{2+}-containing micelles of amphiphilic BCPs.

The ester hydrolase activity of Cu^{2+}-containing micelles was evaluated using p-nitrophenyl picolinate (PNPP) as a model compound.[66] The hydrolysis of PNPP can be catalyzed by Cu^{2+} ions to produce 2-picolinic acid (PA) and 4-nitrophenolate (4NP). 4NP has an absorbance at ~ 400 nm that can provide the reaction kinetics monitored by UV-vis spectroscopy. All reactions were carried out in the phosphate buffer solution (PBS) at a pH of 7.0 and the molar ratio of the substrate to Cu^{2+} ions was kept at 10:1 at 25 °C. Figure 5a shows a non-catalytic reaction of PNPP. No apparent product peak was seen at 400 nm. PNPP is relatively stable with a slow autocatalytic behavior. In presence of P3, there was a fast raise of the peak at 400 nm (**Figure 5b**), suggesting the efficient catalytic conversion of PNPP to 4-nitrophenolate. On contrast, the reactivity of P6-Cu^{2+} was much slower than that of P3 (Figure 4d). The corresponding reaction kinetics was fitted as the first-order reaction. For the non-catalytic reaction, the rate constant (*k*) is 0.17×10^{-2} min^{-1}. The *k* of P6-Cu^{2+} increased to 0.35×10^{-2} min^{-1}, approximately 2

times faster than that of non-catalytic ones, suggesting that Cu^{2+} ions were catalytically active. For P3, the *k* is 4.2×10^{-2} min^{-1}, about 12 time more active than that of P6-Cu^{2+}. With smaller size of polymer micelles, *e.g.,* P1, its *k* reached to 9.3×10^{-2} min^{-1}, about 27 time more active than that of P6-Cu^{2+}. Given that P3-Cu^{2+} and P6-Cu^{2+} have similar micellar sizes, we attributed the 12-fold reactivity enhancement of Cu^{2+} ions to their hydrophobic microenvironment in P3-Cu^{2+} but missed in P6-Cu^{2+}. We also emphasized that, although Cu^{2+} ions were confined within hydrophobic domains for P1 and P3, their first coordination sphere is identical.

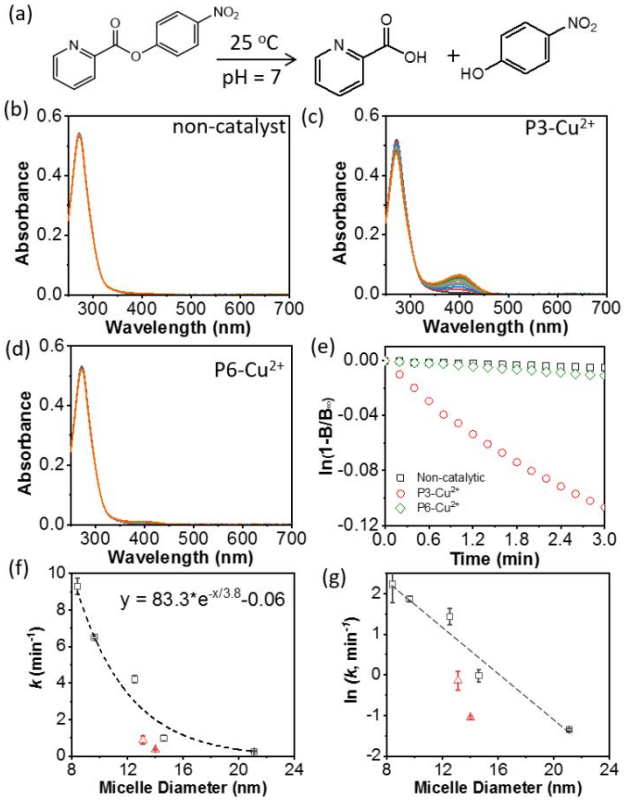

Figure 5. (a) Hydrolysis reaction of PNPP. (b-d) UV-vis spectra to study the hydrolysis of PNPP under: (b) non-catalytic, (c,d) catalyzed by Cu^{2+}-containing micelle of P3 (c) and P6 (d). (e) First-order reaction kinetics for PNPP hydrolysis of non-catalytic reaction, and the reactions catalyzed by Cu^{2+} containing micelles of P1, P3 and P6. (f,g) Reaction rate constant plotted as a function of micelle diameter in normal scale (f) and ln scale (g). The red triangles are from P6 and P7 and the black squares are from P1-P5. Reaction conditions: [PNPP] = 27 μM; [Cu] = 2.7 μM; T = 25 °C. PBS buffer with pH = 7.0.

To confirm the impact of the hydrophobic microenvironment, three sets of control experiments were carried out. First of all, $PDMA_{52}$-DPA-Cu^{2+} without any hydrophobic PS segments displayed a moderate hydrolase activity (Figures 6c and S6). Under the same reaction conditions, it has a *k* of 0.16×10^{-2} min^{-1}, very close to that of non-catalytic reaction. Second, the hydrolase activity was evaluated with different PS chain lengths with the same hydrophilic PDMA block, *e.g.,* P1-P5 (Figure 5f). We found that there was an interesting correlation between the size of micelles and the reactivity of Cu^{2+} ions. P1-Cu^{2+} has the best catalytic reactivity and the activity of Cu^{2+} ions decreased along with the increase of the micellar diameter. The reaction catalyzed by P5-Cu^{2+} has the lowest *k* of 0.26×10^{-2} min^{-1}, about 36-fold slower than that with P1-Cu^{2+}. While the hydrophobic microenvironment shows a positive impact on the reactivity of Cu^{2+} ions, there is an exponential decay of Cu^{2+} reactivity with the increase of the micellar sizes (Figure 5c). Third, with Cu^{2+} ions on the hydrophilic shell, the activity of Cu^{2+} ions do not vary significantly by BCPs.

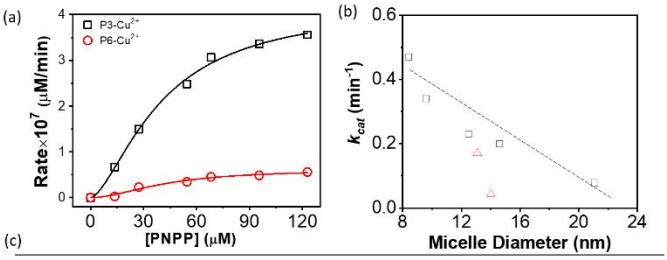

(c)

Entry	Catalyst	$k\times10^2$ (min^{-1})	$V_{max}\times10^7$ (μM/min)	K_M (μM)	k_{cat} (min^{-1})	E_a (KJ/mol)
0	Non-catalytic	0.14 ± 0.025	-	-	-	-
1	$PDMA_{52}$-DPA	0.16 ± 0.045	-	-	-	-
2	$PDMA_{52}$-*b*-PS_{10}-DPA (P1)	9.3 ± 0.45	12.7	38.7	0.47	46.4
3	$PDMA_{52}$-*b*-PS_{30}-DPA (P2)	6.5 ± 0.058	9.2	38.2	0.34	45.1
4	$PDMA_{52}$-*b*-PS_{52}-DPA (P3)	4.2 ± 0.2	6.18	81.7	0.23	43.2
5	$PDMA_{52}$-*b*-PS_{76}-DPA (P4)	0.98 ± 0.15	5.44	120.3	0.20	59.6
6	$PDMA_{52}$-*b*-PS_{105}-DPA (P5)	0.26 ± 0.028	2.12	168.7	0.078	71.0
7	PS_{76}-*b*-$PDMA_{59}$-DPA (P6)	0.35 ± 0.025	1.18	130.1	0.043	64.6
8	PS_{76}-*b*-$PDMA_{89}$-DPA (P7)	0.87 ± 0.23	4.48	92.3	0.17	54.0

Figure 6. (a) Michaelis–Menten plots for PNPP hydrolysis catalyzed by Cu^{2+}-containing micelles of P3 and P6. (b) The plot of micelle diameter vs k_{cat}. The red triangles are from P6 and P7 and the black squares are from P1-P5. (c) Reaction conditions: [PNPP] = 0 to 123 μM; [Cu^{2+}] = 2.7 μM; T = 25 °C. PBS buffer with pH = 7.0. (c) the table to summarize the first order rate constants and fitting results of V_{max}, K_M, k_{cat} from Michaelis–Menten plots for PNPP hydrolysis. E_a was calculated from the Arrhenius Plot.

We further used the Michaelis-Menten model to get insights into how the local hydrophobicity promotes catalytic efficiency of Cu^{2+} ions. The initial rate was considered by varying the concentration of substrates from 14 μM to 122 μM at a constant Cu^{2+} concentration of 2.7 μM. The results are summarized in Figures 6 and S7. The kinetics parameters show a typical non-linear regression with increasing the concentration of PNPP. The Michaelis constant (K_M) is in selected cases an inverse measure of the binding affinity between catalytic Cu^{2+} ions and substrates. For micelles with Cu^{2+} ions in the hydrophobic cores, *e.g.,* P1-P5, K_M increases along with the chain length of PS; that is, the smaller diameter of micelles favors the binding. Additionally, this trend could indicate that the larger micelles are more rigid since similar effects have been observed on the enzymatic activity of PEGylated chymotrypsin conjugates.[67] Interestingly, for P6 and P7 where Cu^{2+} ions reside out of the hydrophobic cores, their K_M is considerably large. Given that the substrate PNPP is relatively hydrophobic, it is reasonable to assume that its local concentration is higher within the micellar cores, as compared to that in the buffer solution.

The maximum velocity (V_{max}) and the turnover frequency per Cu^{2+} site (k_{cat}) describe the zero-order kinetics where an infinite amount of substrate is available for the initial turnover. Note k_{cat} is slightly high than the rate constant *k*, because it only takes accounts of the initial reaction rate. The activity of Cu^{2+}, both k_{cat}, and V_{max}, is also dependent on the chain length of PS or the diameter of polymer micelles (Figure 6b). The k_{cat} and V_{max} of P1-Cu^{2+} are about 6-times higher than that of P5-Cu^{2+}. However, the decay of k_{cat} on the diameter of micelles is much slow (Figure 6b), as compared to that of the overall rate constant *k* (Figure 5f). Those results suggests that, by confining Cu^{2+} sites in the hydrophobic cores, their overall kinetic performances are benefited from their thermodynamic binding

enhancement, likely as the rate-determining step. This conclusion is also supported by the activation energy calculated from the Arrhenius plot (Figure S8). For P4 and P5, the activation energy barrier increased by 30%-40% as compared to that of P1-P3.

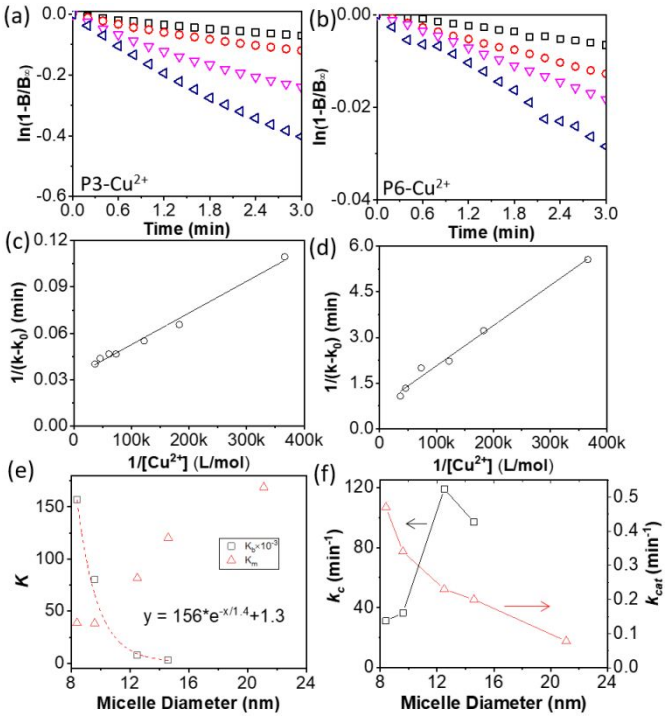

Figure 7. Saturation kinetics plots of PNPP hydrolysis catalyzed by Cu^{2+} containing micelle of (a) P3-Cu^{2+} and (b) P6-Cu^{2+}. And fitting plots of PNPP hydrolysis catalyzed by Cu^{2+} containing micelle of (c) P3-Cu^{2+} and (d) P6-Cu^{2+}. (e) K_b and K_M plotted as a function of the micellar diameter. (f) k_c and k_{cat} plotted as a function of the micellar diameter. Reaction conditions: [PNPP] = 27 μM; [Cu^{2+}] = 1.4 to 27 μM; T = 25 °C; PBS buffer at pH = 7.0.

To quantitatively access the binding constant (K_b), we further carried out the reverse saturation kinetics behavior, *i.e.,* by increasing the ratio of catalyst-to-substrate. The first-order rate constant was measured at different concentrations of Cu^{2+} ion in the range of 1.4 at a constant concentration of PNPPM. By solving the numeric formation rate of 4NP in eqs 1-4, the binding constant (K_b) can be obtained by fitting the reciprocal catalyst concentration *1/[Cu²⁺]* and *1/(k_{obs}-k_0),* as follows.

$$Non-catalytic: \quad [S] \xrightarrow{k_0} [PA] + [4NP] \qquad eq\ 1$$

$$Catalytic: \quad [S] + [Cu^{2+}] \xrightarrow{k_{obs}} [PA] + [4NP] + [Cu^{2+}] \qquad eq\ 2$$

$$[Cu^{2+}] + [S] \overset{K_b}{\leftrightarrow} [Cu^{2+} - S] \xrightarrow{k_c} [Cu^{2+} - PA] + [4NP] \rightarrow [Cu^{2+}] + [PA]$$

$$\frac{1}{k_{obs} - k0} = \frac{1}{kc - k0} + \frac{1}{(kc - k0)K_b} \times \frac{1}{[Cu^{2+}]} \qquad eq\ 4$$

where k (min^{-1}) is the measured rate constant at different concentrations of Cu^{2+} ions; k_0 (min^{-1}) is the non-catalytic rate constant; k_c is the catalytic rate constant of bound substrates per Cu^{2+} per minute; K_b is the bonding constant between the substrate and Cu^{2+}-containing polymer micelles. Those results are summarized in Figure 7. Using P3-Cu^{2+} and P6-Cu^{2+} as examples, the reactions rate increased obviously with the increase of the ratio of catalyst-to-substrate (Figure 7a and b). The rate constant increased much faster in P3-Cu^{2+}. When the molar ratio of catalyst-to-substrate is 1:1, the reaction with P3-Cu^{2+} is 30-fold faster than that with P6-Cu^{2+}. It further confirms the difference of catalytic performance is derived from the topologies of micelles. The observed rate constant (k_{obs}) shows a non-linear procession along the ratio of catalyst-to-substrate, suggesting that the reaction is limited by binding of the substrate to the catalytic site. At a high catalyst-to-substrate ratio where each Cu^{2+} only shows close to one turnover, the initial binding rate limits the overall reaction rate. For example, after the catalyst-to-substrate ratio reaches to 0.4, the further increase of the rate constant tended to slow down the reactions with P3-Cu^{2+}. A similar trend was seen for P1 and P2 with a high reactivity.

When plotting 1/[Cu^{2+}] as a function of 1/(k-k_0) (Figure 7c), the typical fitting results of P3-Cu^{2+} and P6-Cu^{2+} are shown in Figures 7c and 7d. For the slop and intercept, the binding constant K_b of P3-Cu^{2+} is 7.9 $\times 10^3$ M^{-1} and the catalytic rate constant (k_c) is 119 min^{-1}. The results of K_b for P1-P4 are summarized in Figure 7e. When confining Cu^{2+} ions within small micelles, the K_b is significantly larger as compared to those without hydrophobic cores. For P1-Cu^{2+}, its K_b with the substrate is 157×10^3 μM^{-1}, that is about 52-times higher than that of P4-Cu^{2+} and 23-times higher than that of P6-Cu^{2+}. (Figures S9-S10) We note that, P5-Cu^{2+} and P7-Cu^{2+} cannot be fitted with this model because their binding constants are too small, implying that the initial binding is unfavorable under those reaction conditions. The decrease of K_b tracks the trend of K_M, indicating that for this class of enzyme mimics the latter term can be approximated to a binding constant.

Quantitatively, the K_b decays exponentially with the size of micelles (d) as $K_b \propto e^{-d}$. As the K_b is dependent on both local concentrations of Cu^{2+} and substrates, the increase of the micellar sizes would decrease the number density of Cu^{2+} ions per unit volume (Table 1). Despite of the hydrophobicity enhanced the solubility of PNPP, the overall trend of K_b is dominated by the number density of Cu^{2+} ions. As compared P1 with P3, the increase of micellar sizes from 8.4 nm to 21.2 nm led to the decrease of Cu^{2+} concentration per unit volume. We estimated the concentration of Cu^{2+} ions per unit volume of micelle cores, *i.e.,* quotient of the average aggregation number (N_{agg}) and the volume of micellar cores (Table 1). The number of Cu^{2+} ions per nm^3 decreases from 0.6 nm^{-3} for P1 to 0.06 nm^{-3} for P5. Therefore, hydrophobic microenvironment with perfect dimensions can significantly improve the binding affinity; however, the large hydrophobic cores of polymer micelles would create thermodynamic barriers to limit the binding of substrates and Cu^{2+} sites. The decrease of K_d is on the same magnitude with the decrease of the number density of Cu^{2+} ions, suggesting the decrease of the local concentration of Cu^{2+} ions to be correlative with the binding depression. However, for large micelles like P3-Cu^{2+} and P6-Cu^{2+}, the K_b is almost identical. The improvement of catalytic efficiency is therefore only from hydrophobicity-enhanced binding of substrates and Cu^{2+} ions.

We further analyzed the catalytic rate constant (k_c) measured from saturation kinetics. Although in many cases k_c is kinetically identical to k_{cat}, k_c reflects the true first-order kinetics at a much lower substrate concentration and k_c does not consider the dissociation of products from Cu^{2+} sites. Without true turnover, k_c is significantly larger than k_{cat}. Interestingly, we note that, P3-Cu^{2+} and P6-Cu^{2+} had very close K_b at a similar ratio of catalyst-to-substrate; but the k_c of P3-Cu^{2+} is about 20-times greater than that of P6-Cu^{2+}. In the reverse saturation kinetics model, the k_c is determined from the extrapolating at an infinite [Cu^{2+}]; so, the k_c only considers the rate from bound substrates (as the sole reactant) to bound products

(and it cannot be results from the dissociation of products in our experiments) without the interfacing of water accessibility. For P1-P4, we observe a positive correlation between k_c and micelle size, in contrast to what we observe for k, k_{cat} and k_{cat}/K_M. The k_c follows an increasing trend with the chain length of PS, *e.g.,* k_c of P3 and P4 is 3-4 times higher than that of P1 and P2. Without hydrophobicity, the k_c of P6-Cu^{2+} decreased dramatically as large as 20-fold, compared to that of P3-Cu^{2+}. Those results suggest that the conversion of Cu^{2+}-substrate to Cu^{2+}-product is faster, i) in hydrophobic cores as compared to hydrophilic ones; and ii) in larger micelles as compared to smaller ones. The increase of k_c is likely due to the change of the intrinsic activity of Cu^{2+} ions at a mediate with a low dielectric constant, as a positive kinetic impact of hydrophobic domains. It has been suggested that the nucleophilic attack of water to esters could be improved under hydrophobic microenvironment using hydrophobic surface[68] or nanocavity[69] in a manner akin to enzymes.[70]

The difference in trends of k, k_c and k_{cat}/K_M which reports from the encounter of substrates and catalyst up to the first irreversible step, in our case the step reflected on k_c, can be traced back to the limited accessibility of water within the hydrophobic environment. For k_c, we treat Cu^{2+} sites as a reactant to examine the conversion of bound substrates to bound products. It reports the true hydrophobic impact of this chemical transformation. The k_{cat}/K_M values range from 331 $M^{-1}s^{-1}$ to 12 100 $M^{-1}s^{-1}$ for these Cu^{2+}-containing mimics (Figure S11). For a similar ester hydrolysis reaction, that is the cleavage of a *p*-nitrophenyl ester, a computationally designed enzyme exhibits a catalytic efficiency, k_{cat}/K_M, of 400 $M^{-1}s^{-1}$.[71] In other words, our minimalistic approach using polymeric micelles can recapitulate the efficient activity of enzymes taking advantage of less sophisticated chemical structures as featured in enzymatic frameworks. Clearly, the little understood hydrophobic effect has a large impact on catalysis both in enzymes as well as the design of synthetic mimics. Within the active site, the contribution of dispersion energies and the lack of outer solvation shells interacting with randomized bulk solvent molecules are important factors that can lead to efficient catalysis. It is possible that primeval enzymes took advantage of this feature as it minimalizes the number of catalytic elements while leading to efficient reactions. Therefore, further studies of these systems will provide valuable insights to understand one of the key rules of life as well as aid in the development of robust catalysts.

3. Conclusions

In summary, we demonstrate hydrophobicity-enhanced Cu^{2+} reactivity as an ester hydrolase. We designed two sets of amphiphilic BCPs with precise control of the metal-ligand active sites in/out of the hydrophobic domains during micellization. Using a DPA-containing RAFT CTA, the synthetic sequence, either hydrophobic or hydrophilic first, was used to vary the physical location of the binding motif, DPA; therefore, the hydrophobicity of Cu^{2+} sites. Monodispersed spherical micelles of PS-*b*-PDMA were prepared through thermal annealing in methanol where PS aggregates form hydrophobic cores stabilized by hydrophobic PDMA. The binding motif DPA confine the Cu^{2+} sites to defined microenvironment as confirmed by SAXS and NMR titrations. The hydrophobicity of Cu^{2+} sites within the hydrophobic domain showed a significant impact on their catalytic efficiency towards ester hydrolysis. With P1 having a diameter of 8.4 nm, there was a reactivity enhancement by 12 times as compared to that of P6 with hydrophilic Cu^{2+} sites and 36 times as compared to that of P5 with hydrophobic Cu^{2+} sites but a micellar diameter of 21 nm. We used two different kinetic models, including Michaelis-Menten model and the reverse saturation kinetics model, to understand the impact of hydrophobicity on Cu^{2+} reactivity. The Michaelis constant K_M and the binding constant K_b suggested that hydrophobicity favors the binding of substrates to Cu^{2+} sites at polymer micelles with smaller sizes; however, they decayed exponentially with micellar diameters. A higher thermodynamic barrier was found with increasing the PS molecular weight using Arrhenius analysis. With the reverse saturation kinetics at a high ratio of catalyst-to-substrate, hydrophobicity was found to have a profound impact on the catalytic rate constant k_c. Compared to micelles with similar sizes, there was a 16-20-times kinetic enhancement in the hydrolase activity. Our results on how the hydrophobic domains of Cu micelle impact the catalytic efficiency of metal sites show the importance of hydrophobic pockets in the design of molecular mimics of metalloenzymes and illustrate a promising way toward the design of bioinspired polymeric catalysts.

Conflicts of interest

There are no conflicts to declare.

Acknowledgement

J.H. and A.M.A.-B. are grateful for the support from the National Science Foundation (CBET-2029215 to J.H. and CHE-1652606 to A.M.A.-B.). This is also partially supported by the Research Excellence Program (REP) at the University of Connecticut (UCONN) and the IMMP project at the Institute of Materials Science, UCONN. The authors thank to the beamtime of 16ID-LiX at the NSLS-II (Brookhaven National Lab) through a beamtime proposal (BAG-302208) for the SAXS measurements. The LiX beamline is part of the Center for BioMolecular Structure (CBMS), which is primarily supported by the National Institutes of Health, National Institute of General Medical Sciences (NIGMS) through a P30 Grant (P30GM133893), and by the DOE Office of Biological and Environmental Research (KP1605010). LiX also received additional support from NIH Grant S10 OD012331. As part of NSLS-II, a national user facility at Brookhaven National Laboratory, work performed at the CBMS is supported in part by the U.S. Department of Energy, Office of Science, Office of Basic Energy Sciences Program under contract number DE-SC0012704.

References

1. Breslow, R.; Bandyopadhyay, S.; Levine, M.; Zhou, W., Water Exclusion and Enantioselectivity in Catalysis. *ChemBioChem* **2006,** *7*, 1491-1496.

2. Maren, T. H., Carbonic Anhydrase: Chemistry, Physiology, and Inhibition. *Physiol. Rev.* **1967,** *47*, 595-781.

3. Eady, R. R.; Postgate, J. R., Nitrogenase. *Nature* **1974,** *249*, 805-810.

4. Vallee, B. L.; Williams, R., Metalloenzymes: The Entatic Nature of Their Active Sites. *Proceedings of the National Academy of Sciences* **1968,** *59*, 498-505.

5. Frey, P. A., Review: Strong Hydrogen Bonding in Molecules and Enzymatic Complexes. *Magn Reson Chem* **2001,** *39*, S190-S198.

6. Guo, H.; Salahub, D. R., Cooperative Hydrogen Bonding and Enzyme Catalysis. *Angew. Chem., Int. Ed. Engl.* **1998,** *37*, 2985-2990.

7. Fierke, C. A.; Calderone, T. L.; Krebs, J. F., Functional Consequences of Engineering the Hydrophobic Pocket of Carbonic Anhydrase Ii. *Biochemistry* **1991,** *30*, 11054-11063.
8. Walther, M.; Wiesner, R.; Kuhn, H., Investigations into Calcium-Dependent Membrane Association of 15-Lipoxygenase-1: Mechanistic Roles of Surface-Exposed Hydrophobic Amino Acids and Calcium. *J. Biol. Chem.* **2004,** *279*, 3717-3725.
9. Soucy, T. L.; Dean, W. S.; Zhou, J.; Rivera Cruz, K. E.; McCrory, C. C. L., Considering the Influence of Polymer–Catalyst Interactions on the Chemical Microenvironment of Electrocatalysts for the Co2 Reduction Reaction. *Acc. Chem. Res.* **2022,** *55*, 252-261.
10. Pham, T. H. M.; Zhang, J.; Li, M.; Shen, T.-H.; Ko, Y.; Tileli, V.; Luo, W.; Züttel, A., Enhanced Electrocatalytic Co2 Reduction to C2+ Products by Adjusting the Local Reaction Environment with Polymer Binders. *Adv. Energy Mater.* **2022,** *12*, 2103663.
11. Dydio, P.; Key, H.; Nazarenko, A.; Rha, J.-E.; Seyedkazemi, V.; Clark, D.; Hartwig, J., An Artificial Metalloenzyme with the Kinetics of Native Enzymes. *Science* **2016,** *354*, 102-106.
12. La Sorella, G.; Strukul, G.; Scarso, A., Recent Advances in Catalysis in Micellar Media. *Green. Chem.* **2015,** *17*, 644-683.
13. Witte, F. M.; Engberts, J. B., Micelle—Polymer Complexes: Aggregation Numbers, Micellar Rate Effects and Factors Determining the Complexation Process. *Colloids Surf.* **1989,** *36*, 417-426.
14. Yonezawa, T.; Toshima, N., Polymer-and Micelle-Protected Gold/Platinum Bimetallic Systems. Preparation, Application to Catalysis for Visible-Light-Induced Hydrogen Evolution, and Analysis of Formation Process with Optical Methods. *J. Mol. Catal.* **1993,** *83*, 167-181.
15. Zhang, L.; Wei, Z.; Thanneeru, S.; Meng, M.; Kruzyk, M.; Ung, G.; Liu, B.; He, J., A Polymer Solution to Prevent Nanoclustering and Improve the Selectivity of Metal Nanoparticles for Electrocatalytic Co2 Reduction. *Angew. Chem., Int. Ed. Engl.* **2019,** *131*, 15981-15987.
16. Zhang, L.; Wei, Z.; Meng, M.; Ung, G.; He, J., Do Polymer Ligands Block the Catalysis of Metal Nanoparticles? Unexpected Importance of Binding Motifs in Improving Catalytic Activity. *J. Mater. Chem. A* **2020,** *8*, 15900-15908.
17. Bergbreiter, D. E., Soluble Polymers as Tools in Catalysis. *ACS Macro Lett.* **2014,** *3*, 260-265.
18. Levy, A.; Feinstein, R.; Diesendruck, C. E., Mechanical Unfolding and Thermal Refolding of Single-Chain Nanoparticles Using Ligand–Metal Bonds. *J. Am. Chem. Soc.* **2019,** *141*, 7256-7260.
19. Rothfuss, H.; Knöfel, N. D.; Roesky, P. W.; Barner-Kowollik, C., Single-Chain Nanoparticles as Catalytic Nanoreactors. *J. Am. Chem. Soc.* **2018,** *140*, 5875-5881.
20. Bohlen, J. L.; Kulendran, B.; Rothfuss, H.; Barner-Kowollik, C.; Roesky, P. W., Heterobimetallic Au (I)/Y (Iii) Single Chain Nanoparticles as Recyclable Homogenous Catalysts. *Polymer Chemistry* **2021,** *12*, 4016-4021.
21. Thanneeru, S.; Nganga, J. K.; Amin, A. S.; Liu, B.; Jin, L.; Angeles-Boza, A. M.; He, J., "Enzymatic" Photoreduction of Carbon Dioxide Using Polymeric Metallofoldamers Containing Nickel–Thiolate Cofactors. *ChemCatChem* **2017,** *9*, 1157-1162.
22. Jin, L.; Thanneeru, S.; Cintron, D.; He, J., Bioinspired Design of Hybrid Polymer Catalysts with Multicopper Sites for Oxygen Reduction. *ChemCatChem* **2020,** *12*, 5932-5937.
23. Chen, J.; Wang, J.; Bai, Y.; Li, K.; Garcia, E. S.; Ferguson, A. L.; Zimmerman, S. C., Enzyme-Like Click Catalysis by a Copper-Containing Single-Chain Nanoparticle. *J Am Chem Soc* **2018,** *140*, 13695-13702.
24. Karayilan, M.; Brezinski, W. P.; Clary, K. E.; Lichtenberger, D. L.; Glass, R. S.; Pyun, J., Catalytic Metallopolymers from [2fe-2s] Clusters: Artificial Metalloenzymes for Hydrogen Production. *Angewandte Chemie* **2019**.
25. Rothfuss, H.; Knofel, N. D.; Roesky, P. W.; Barner-Kowollik, C., Single-Chain Nanoparticles as Catalytic Nanoreactors. *J Am Chem Soc* **2018,** *140*, 5875-5881.
26. Rubio-Cervilla, J.; González, E.; Pomposo, J. A., Advances in Single-Chain Nanoparticles for Catalysis Applications. *Nanomaterials* **2017,** *7*.
27. Liu, Y.; Pujals, S.; Stals, P. J.; Paulöhrl, T.; Presolski, S. I.; Meijer, E.; Albertazzi, L.; Palmans, A. R., Catalytically Active Single-Chain Polymeric Nanoparticles: Exploring Their Functions in Complex Biological Media. *J Am Chem Soc* **2018,** *140*, 3423-3433.
28. Hanlon, A. M.; Lyon, C. K.; Berda, E. B., What Is Next in Single-Chain Nanoparticles? *Macromolecules* **2016,** *49*, 2-14.
29. Chen, R.; Berda, E. B., 100th Anniversary of Macromolecular Science Viewpoint: Re-Examining Single-Chain Nanoparticles. *Acs Macro Lett* **2020,** *9*, 1836-1843.
30. Kirkorian, K.; Ellis, A.; Twyman, L. J., Catalytic Hyperbranched Polymers as Enzyme Mimics; Exploiting the Principles of Encapsulation and Supramolecular Chemistry. *Chem. Soc. Rev.* **2012,** *41*, 6138-6159.
31. Astruc, D.; Chardac, F., Dendritic Catalysts and Dendrimers in Catalysis. *Chem. Rev.* **2001,** *101*, 2991-3024.
32. McKay, C. S.; Finn, M., Polyvalent Catalysts Operating on Polyvalent Substrates: A Model for Surface-Controlled Reactivity. *Angewandte Chemie International Edition* **2016,** *55*, 12643-12649.
33. Delort, E.; Darbre, T.; Reymond, J.-L., A Strong Positive Dendritic Effect in a Peptide Dendrimer-Catalyzed Ester Hydrolysis Reaction. *J Am Chem Soc* **2004,** *126*, 15642-15643.
34. Fersht, A., *Structure and Mechanism in Protein Science: A Guide to Enzyme Catalysis and Protein Folding*. Macmillan: 1999.
35. Artar, M. g.; Souren, E. R. J.; Terashima, T.; Meijer, E. W.; Palmans, A. R. A., Single Chain Polymeric Nanoparticles as Selective Hydrophobic Reaction Spaces in Water. *Acs Macro Lett* **2015,** *4*, 1099-1103.
36. Stals, P. J. M.; Cheng, C.-Y.; van Beek, L.; Wauters, A. C.; Palmans, A. R. A.; Han, S.; Meijer, E. W., Surface Water Retardation around Single-Chain Polymeric Nanoparticles: Critical for Catalytic Function? *Chem Sci* **2016,** *7*, 2011-2015.
37. Ren, F. Y.; Chen, K.; Qiu, L. Q.; Chen, J. M.; Darensbourg, D. J.; He, L. N., Amphiphilic Polycarbonate Micellar Rhenium Catalysts for Efficient Photocatalytic Co2 Reduction in Aqueous Media. *Angew. Chem., Int. Ed. Engl.* **2022,** *134*, e202200751.
38. Lipshutz, B. H.; Taft, B. R., Heck Couplings at Room Temperature in Nanometer Aqueous Micelles. *Org. Lett.* **2008,** *10*, 1329-1332.
39. Menger, F.; Gan, L.; Johnson, E.; Durst, D., Phosphate Ester Hydrolysis Catalyzed by Metallomicelles. *J. Am. Chem. Soc.* **1987,** *109*, 2800-2803.
40. Gellman, S. H.; Petter, R.; Breslow, R., Catalytic Hydrolysis of a Phosphate Triester by Tetracoordinated Zinc Complexes. *J. Am. Chem. Soc.* **1986,** *108*, 2388-2394.
41. Fornasier, R.; Scrimin, P.; Tecilla, P.; Tonellato, U., Bolaform and Classical Cationic Metallomicelles as Catalysts of the Cleavage of P-Nitrophenyl Picolinate. *Journal of the American Chemical Society* **1989,** *111*, 224-229.
42. Polyzos, A.; Hughes, A. B.; Christie, J. R., Catalysis of Aryl Ester Hydrolysis in the Presence of Metallomicelles Containing a Copper (Ii) Diethylenetriamine Derivative. *Langmuir* **2007,** *23*, 1872-1879.
43. Li, J.; Han, J.; Lin, Z.; Tang, L.; Huang, Q.; Wang, Q.; Zhu, J.; Deng, J., Influence Factors Studies on the Rh-Catalyzed Asymmetric Transfer Hydrogenation of Ketones with Surfactant-Type Ligand in Water. *Tetrahedron* **2019,** *75*, 422-428.

44. Li, J.; Zhang, Y.; Han, D.; Jia, G.; Gao, J.; Zhong, L.; Li, C., Transfer Hydrogenation of Aldehydes on Amphiphilic Catalyst Assembled at the Interface of Emulsion Droplets. *Green. Chem.* **2008,** *10*, 608-611.
45. Tang, S.; Li, L.; Ren, X.; Li, J.; Yang, G.; Li, H.; Yuan, B., Metallomicelle Catalyzed Aerobic Tandem Desilylation/Glaser Reaction in Water. *Green. Chem.* **2019,** *21*, 2899-2904.
46. Banerjee, M.; Panjikar, P. C.; Bhutia, Z. T.; Bhosle, A. A.; Chatterjee, A., Micellar Nanoreactors for Organic Transformations with a Focus on "Dehydration" Reactions in Water: A Decade Update. *Tetrahedron* **2021,** *88*, 132142.
47. Thanneeru, S.; Milazzo, N.; Lopes, A.; Wei, Z.; Angeles-Boza, A. M.; He, J., Synthetic Polymers to Promote Cooperative Cu Activity for O2 Activation: Poly Vs Mono. *J. Am. Chem. Soc.* **2019,** *141*, 4252-4256.
48. McKay, C. S.; Finn, M., Polyvalent Catalysts Operating on Polyvalent Substrates: A Model for Surface-Controlled Reactivity. *Angew. Chem., Int. Ed. Engl.* **2016,** *128*, 12833-12839.
49. Bergbreiter, D., Acs Macro Lett. 2014, 3, 260− 265; B) De Bergbreiter, Thermomorphic Catalysts. *Recoverable and Recyclable Catalysts; Benaglia, M., Ed.; John Wiley & Sons: Chichester, UK* **2009**.
50. Prins, L. J.; Mancin, F.; Scrimin, P., Multivalent Cooperative Catalysts. *Current Organic Chemistry* **2009,** *13*, 1050-1064.
51. Delort, E.; Darbre, T.; Reymond, J.-L., A Strong Positive Dendritic Effect in a Peptide Dendrimer-Catalyzed Ester Hydrolysis Reaction. *J. Am. Chem. Soc.* **2004,** *126*, 15642-15643.
52. Suh, J.; Hah, S. S., Organic Artificial Proteinase with Active Site Comprising Three Salicylate Residues. *J. Am. Chem. Soc.* **1998,** *120*, 10088-10093.
53. Lambert, R.; Wirotius, A.-L.; Vignolle, J.; Taton, D., C–C Couplings in Water by Micellar Catalysis at Low Loadings from a Recyclable Polymer-Supported Pd(Ii)–Nhc Nanocatalyst. *Polym. Chem.* **2019,** *10*, 460-466.
54. Wang, D.; Astruc, D., The Recent Development of Efficient Earth-Abundant Transition-Metal Nanocatalysts. *Chem Soc Rev* **2017,** *46*, 816-854.
55. Deraedt, C.; Salmon, L.; Etienne, L.; Ruiz, J.; Astruc, D., "Click" Dendrimers as Efficient Nanoreactors in Aqueous Solvent: Pd Nanoparticle Stabilization for Sub-Ppm Pd Catalysis of Suzuki–Miyaura Reactions of Aryl Bromides. *Chem comm* **2013,** *49*, 8169-8171.
56. Handa, S.; Wang, Y.; Gallou, F.; Lipshutz, B. H., Sustainable Fe–Ppm Pd Nanoparticle Catalysis of Suzuki-Miyaura Cross-Couplings in Water. *Science* **2015,** *349*, 1087-1091.
57. Schönfelder, D.; Fischer, K.; Schmidt, M.; Nuyken, O.; Weberskirch, R., Poly(2-Oxazoline)S Functionalized with Palladium Carbene Complexes: Soluble, Amphiphilic Polymer Supports for C−C Coupling Reactions in Water. *Macromolecules* **2005,** *38*, 254-262.
58. Aamer, K. A.; Tew, G. N., Synthesis of Terpyridine-Containing Polymers with Blocky Architectures. *Macromolecules* **2004,** *37*, 1990-1993.
59. Qu, P.; Kuepfert, M.; Jockusch, S.; Weck, M., Compartmentalized Nanoreactors for One-Pot Redox-Driven Transformations. *ACS Catalysis* **2019,** *9*, 2701-2706.
60. Zayas, H. A.; Lu, A.; Valade, D.; Amir, F.; Jia, Z.; O'Reilly, R. K.; Monteiro, M. J., Thermoresponsive Polymer-Supported L-Proline Micelle Catalysts for the Direct Asymmetric Aldol Reaction in Water. *ACS Macro Lett.* **2013,** *2*, 327-331.
61. Wei, Z.; Liu, C.-H.; Duan, H.; Luo, Q.; Huang, M.; Thanneeru, S.; Nieh, M.-P.; He, J., Self-Assembly of Gold Nanoparticles Grafted with Amphiphilic Supramolecular Block Copolymers. *Giant* **2022,** *10*, 100102.
62. Wei, Z.; Duan, H.; Weng, G.; He, J., Metals in Polymers: Hybridization Enables New Functions. *J. Mater. Chem. C* **2020,** *8*, 15956-15980.
63. LaRue, I.; Adam, M.; Zhulina, E. B.; Rubinstein, M.; Pitsikalis, M.; Hadjichristidis, N.; Ivanov, D. A.; Gearba, R. I.; Anokhin, D. V.; Sheiko, S. S., Effect of the Soluble Block Size on Spherical Diblock Copolymer Micelles. *Macromolecules* **2008,** *41*, 6555-6563.
64. Hansen, J.-P.; Hayter, J. B., A Rescaled Msa Structure Factor for Dilute Charged Colloidal Dispersions. *Mol. Phys.* **1982,** *46*, 651-656.
65. Hayter, J. B.; Penfold, J., An Analytic Structure Factor for Macroion Solutions. *Mol. Phys.* **1981,** *42*, 109-118.
66. Xiang, Y.; Zeng, X.; Cheng, S.; Li, Y.; Xie, J., Metallomicellar Catalysis Cleavage of P-Nitrophenyl Picolinate Catalyzed by Binuclear Metal Complexes Coordinating Tripeptide in Ctab Micellar Solution. *J. Colloid Interface Sci.* **2001,** *235*, 114-118.
67. Rodríguez-Martínez, J. A.; Rivera-Rivera, I.; Solá, R. J.; Griebenow, K., Enzymatic Activity and Thermal Stability of Peg-A-Chymotrypsin Conjugates. *Biotechnol. Lett.* **2009,** *31*, 883-887.
68. Miura, H.; Kameyama, S.; Komori, D.; Shishido, T., Quantitative Evaluation of the Effect of the Hydrophobicity of the Environment Surrounding Brønsted Acid Sites on Their Catalytic Activity for the Hydrolysis of Organic Molecules. *J. Am. Chem. Soc.* **2018,** *141*, 1636-1645.
69. Bose, I.; Zhao, Y., Selective Hydrolysis of Aryl Esters under Acidic and Neutral Conditions by a Synthetic Aspartic Protease Mimic. *ACS catalysis* **2021,** *11*, 3938-3942.
70. Dorovska, V. N.; Varfolomeyev, S. D.; Kazanskaya, N. F.; Klyosov, A. A.; Martinek, K., The Influence of the Geometric Properties of the Active Centre on the Specificity of A-Chymotrypsin Catalysis. *FEBS Letters* **1972,** *23*, 122-124.
71. Richter, F.; Blomberg, R.; Khare, S. D.; Kiss, G.; Kuzin, A. P.; Smith, A. J.; Gallaher, J.; Pianowski, Z.; Helgeson, R. C.; Grjasnow, A., Computational Design of Catalytic Dyads and Oxyanion Holes for Ester Hydrolysis. *J. Am. Chem. Soc.* **2012,** *134*, 16197-16206.